HHS Public Access

Author manuscript

Magn Reson Med. Author manuscript; available in PMC 2025 May 29.

Published in final edited form as:

Magn Reson Med. 2024 October ; 92(4): 1310–1322. doi:10.1002/mrm.30200.

Accelerated 3D metabolite T_1 mapping of the brain using variable-flip-angle SPICE

Yibo Zhao[1,2], **Yudu Li**[1,3], **Rong Guo**[1,4], **Wen Jin**[1,2], **Brad Sutton**[1,3,5], **Chao Ma**[6], **Georges El Fakhri**[6], **Yao Li**[7,8], **Jie Luo**[7], **Zhi-Pei Liang**[1,2]

[1]Beckman Institute for Advanced Science and Technology, University of Illinois at Urbana-Champaign, Urbana, Illinois, USA

[2]Department of Electrical and Computer Engineering, University of Illinois at Urbana-Champaign, Urbana, Illinois, USA

[3]National Center for Supercomputing Applications, University of Illinois at Urbana-Champaign, Urbana, Illinois, USA

[4]Siemens Medical Solutions USA, Inc., Urbana, Illinois, USA

[5]Department of Bioengineering, University of Illinois at Urbana-Champaign, Urbana, Illinois, USA

[6]Department of Radiology and Biomedical Imaging, Yale University School of Medicine, New Haven, Connecticut, USA

[7]School of Biomedical Engineering, Shanghai Jiao Tong University, Shanghai, China

[8]Institute of Medical Robotics, Shanghai Jiao Tong University, Shanghai, China

Abstract

Purpose: To develop a practical method to enable 3D T_1 mapping of brain metabolites.

Theory and Methods: Due to the high dimensionality of the imaging problem underlying metabolite T_1 mapping, measurement of metabolite T_1 values has been currently limited to a single voxel or slice. This work achieved 3D metabolite T_1 mapping by leveraging a recent ultrafast MRSI technique called SPICE (spectroscopic imaging by exploiting spatiospectral correlation). The Ernst-angle FID MRSI data acquisition used in SPICE was extended to variable flip angles, with variable-density sparse sampling for efficient encoding of metabolite T_1 information. In data processing, a novel generalized series model was used to remove water and subcutaneous lipid signals; a low-rank tensor model with prelearned subspaces was used to reconstruct the variable-flip-angle metabolite signals jointly from the noisy data.

Correspondence: Zhi-Pei Liang, Department of Electrical and Computer Engineering, Beckman Institute for Advanced Science and Technology, University of Illinois at Urbana-Champaign, 405 N. Mathews Ave, Urbana, IL 61801, USA. z-liang@illinois.edu.

CONFLICT OF INTEREST

R.G. is currently employed by Siemens Medical Solutions USA, Inc. The other authors declare no competing interests.

SUPPORTING INFORMATION

Additional supporting information may be found in the online version of the article at the publisher's website.

Results: The proposed method was evaluated using both phantom and healthy subject data. Phantom experimental results demonstrated that high-quality 3D metabolite T_1 maps could be obtained and used for correction of T_1 saturation effects. In vivo experimental results showed metabolite T_1 maps with a large spatial coverage of 240 × 240 × 72 mm^3 and good reproducibility coefficients (< 11%) in a 14.5-min scan. The metabolite T_1 times obtained ranged from 0.99 to 1.44 s in gray matter and from 1.00 to 1.35 s in white matter.

Conclusion: We successfully demonstrated the feasibility of 3D metabolite T_1 mapping within a clinically acceptable scan time. The proposed method may prove useful for both T_1 mapping of brain metabolites and correcting the T_1-weighting effects in quantitative metabolic imaging.

Keywords

FID MRSI; low-rank tensor modeling; metabolite T_1 mapping; variable flip angle

1 | INTRODUCTION

MRSI has been used for noninvasive measurement and quantification of several endogenous metabolites (e.g., N-acetylaspartate [NAA], creatine [Cr], and choline [Cho]) of the brain. The measured metabolite signals are, however, often weighted by the T_1 effects, which may complicate the biological interpretation of their changes. The weighting effects become more significant in accelerated MRSI experiments with very short TRs.[1–4] Therefore, to ensure accurate estimation of metabolite concentrations, metabolite T_1 values are needed for correcting the T_1 weighting effects. These values can also be used for optimizing scan parameters[5–9] and providing informative insights into the microenvironment of pathological conditions.[10,11]

Measuring metabolite T_1 values requires acquiring a series of T_1-weighted spectroscopic signals using, such as variable-TR, variable-flip-angle (VFA), or inversion-recovery sequences. This adds another dimension to the imaging problem and exacerbates the challenge of achieving fast imaging with high spatial resolution, large spatial coverage, and good SNR in MRSI experiments. As a result, current technologies for measuring metabolite T_1 values have been limited to single-voxel[5–11] or single-slice[12–14] experiments. To the best of our knowledge, no studies have been reported for 3D metabolite T_1 mapping so far.

Recently, the feasibility of ultrafast 3D MRSI has been demonstrated using SPICE (spectroscopic imaging by exploiting spatiospectral correlation).[1,15–21] In data acquisition, SPICE features an accelerated FID MRSI sequence without water and lipid suppression pulses. Rapid scanning has been accomplished by combining short TR, ultrashort TE, and extended echo-planar spectroscopic imaging trajectories[21,22] to sparsely sample (k,t)-space. In data processing, SPICE leverages a union-of-subspaces model to address the problems of water and lipid removal and metabolite reconstruction from sparse and noisy data. With these advances, SPICE can provide 3D metabolite mapping in several clinical applications, including stroke,[23–25] tumor,[26] Alzheimer's disease,[27] and epilepsy.[28] However, the current SPICE method lacks metabolite T_1 mapping capability; thus, the resulting metabolite signals carry strong T_1-weighting effects due to short-TR (160 ms) acquisition.

This work extends the basic SPICE to VFA SPICE to enable 3D metabolite T_1 mapping. The high-dimensional data space was sampled in variable density, with extended k-space coverage for the Ernst-angle excitations and limited k-space coverage for the non-Ernst-angle excitations. In data processing, a novel generalized series (GS) model was used to remove nuisance signals from the low-resolution non-Ernst-angle MRSI data, which effectively incorporated the high-resolution spatiospectral priors from the Ernst-angle MRSI data; a prelearned low-rank tensor (LRT) model was used to effectively reconstruct the VFA metabolite signals jointly from the noisy data. The proposed technology was evaluated using phantom and in vivo experiments, producing high-quality and reproducible results.

2 | THEORY

2.1 | Data acquisition

The proposed data-acquisition scheme is illustrated in Figure 1A, which maintains the acquisition features of the basic SPICE,[1,20,21] including (1) short-TR (160 ms), ultrashort-TE (1.6 ms), Ernst-flip-angle (27°) FID MRSI; (2) elimination of water and lipid suppression pulses; (3) extended echo-planar spectroscopic imaging readout to cover the (k_x,t)-space and conventional phase encodings to cover the (k_y,k_z)-space; and (4) embedded navigators to monitor subject motion and field drift during the scan.

This basic SPICE sequence was extended to VFA excitations for measuring metabolite T_1 values. The reasons for using VFA instead of inversion-recovery or variable-TR sequences are 2-fold. First, VFA excitations do not affect the short-TR FID acquisition used in the SPICE sequence, which provides high sampling and SNR efficiency. Compared with conventional inversion-recovery or variable-TR spin echo–based MRSI methods with long TR (usually >1.5 s), our proposed scheme provides about 10-fold acceleration. Second, the B_1 sensitivity issue of T_1 mapping using VFA excitations[29] can effectively be addressed in the proposed method using unsuppressed water signals for B_1 estimation.

Five flip angles were used in the proposed sequence (17°/22°/27°/32°/37°) to encode T_1 and B_1 information. Instead of densely sampling all five flip angles as the basic SPICE (with the Ernst-angle excitation), which would result in an excessively long scan time (~35 min), we sampled the (k_y,k_z)-space in variable density to shorten the data acquisition time, as illustrated in Figure 1B. More specifically, for the Ernst-angle excitation with optimal SNR, k-space was sampled with extended coverage (78 × 24 phase encodings, 3.1 × 3.0 mm resolution). For other flip angles, only central k-space data were sampled (24 × 24 phase encodings, 10.0 × 3.0 mm resolution). The limited sampling of other flip angles is feasible, because high-resolution spatial information has been encoded in the Ernst-angle data. Residual signal variations among different flip angles can be well characterized by appropriate T_1-weighting functions, which can be captured by a small number of spatial encodings. In other words, the inherent degrees of freedom (DOF), or number of unknowns, can be significantly reduced by exploiting the correlation among the data of different flip angles, allowing accelerated sampling of the high-dimensional data space. Overall, the proposed variable-density sampling scheme provided a factor of 2.4 acceleration, reducing the total scan time for 3D metabolite T_1 mapping (FOV = 240 × 240 × 72 mm^3) to only 14.5 min.

2.2 | Data processing

We leveraged the SPICE data processing pipeline to process VFA SPICE data, which can effectively remove the lipid and water signals from the high-resolution MRSI data.[30] The remaining data processing problems were (1) removal of water and lipid signals from non-Ernst-angle MRSI data with very limited k-space coverage, and (2) reconstruction of VFA MRSI images from undersampled noisy data.

2.2.1 | Nuisance signals removal: To solve the first problem, we treated the determined high-resolution water and lipid signals as references, and expressed the low-resolution water and lipid signals using the following GS models[31,32]:

$$\begin{aligned}\rho_{\mathrm{L}}\left(\boldsymbol{x},t,\theta\right)&=\sum_{n=-N_{\mathrm{L}}}^{N_{\mathrm{L}}}\alpha_n\left(t,\theta\right)\hat{\rho}_{\mathrm{L}}(\boldsymbol{x},t,\theta_{\mathrm{ref}})e^{-i2\pi n\Delta\boldsymbol{k}\cdot\boldsymbol{x}},\\ \rho_{\mathrm{W}}\left(\boldsymbol{x},t,\theta\right)&=\sum_{n=-N_{\mathrm{W}}}^{N_{\mathrm{W}}}\beta_n\left(\boldsymbol{x},\theta\right)\hat{\rho}_{\mathrm{W}}(\boldsymbol{x},t,\theta_{\mathrm{ref}})e^{-i2\pi n\Delta ft}.\end{aligned} \tag{1}$$

where $\rho_{\mathrm{L}}(\boldsymbol{x},t,\theta)$ and $\rho_{\mathrm{W}}(\boldsymbol{x},t,\theta)$ are the desired lipid and water signals, respectively, both of which are functions of space ($\boldsymbol{x}$), time (t), and flip angle (θ); $\hat{\rho}_{\mathrm{L}}(\boldsymbol{x},t,\theta_{\mathrm{ref}})$ and $\hat{\rho}_{\mathrm{W}}(\boldsymbol{x},t,\theta_{\mathrm{ref}})$ are the high-resolution lipid and water references estimated from Ernst-angle (θ_{ref}) excitation; and $\alpha_n(t,\theta)$ and $\beta_n(\boldsymbol{x},\theta)$ are the GS model coefficients.

The GS model for lipid removal was formulated in the spatial domain because the separation of subcutaneous lipid and metabolite signals is feasible by their spatial orthogonality (i.e., the lipid signals that we aim to remove originate from the subcutaneous region, whereas metabolites are located within the brain). Note that there may be detectable lipid signals originating from the brain tissue under pathological conditions[33–35]; these lipid signals are not removed in this step, as they may contain useful information for lesion characterization. The high-resolution reference provided accurate spatial boundary information and spatial variation information of the lipid signals. The spatial GS model effectively absorbed such spatial information by directly incorporating the reference image into the spatial bases. The modulation function in the GS model, $\sum_{n=-N_{\mathrm{L}}}^{N_{\mathrm{L}}}\alpha_n\left(t,\theta\right)e^{-i2\pi n\Delta\boldsymbol{k}\cdot\boldsymbol{x}}$, was designed to capture the discrepancies between the Ernst-angle and non-Ernst-angle excitations. Such discrepancies can be well characterized by a T_1-weighting modulation effect $s_{\mathrm{L}}(\boldsymbol{x},t,\theta)$, which is known to contain primarily low-frequency information[36] and can be well approximated by a truncated Fourier series as follows:

$$S_{\mathrm{L}}\left(\boldsymbol{x},t,\theta\right)\approx\sum_{n=-N_{\mathrm{L}}}^{N_{\mathrm{L}}}\alpha_n\left(t,\theta\right)e^{-i2\pi n\Delta\boldsymbol{k}\cdot\boldsymbol{x}}, \tag{2}$$

resulting in the modulation functional in the proposed spatial GS model. Because N_{L} is a much smaller number than the number of voxels to be reconstructed, the proposed GS

model leads to significant reduction in DOF. In practice, we have found $N_L = 15 \times 15$ to be sufficient for representing lipid signals, making it possible for determination of lipid signals from limited k-space data with 24 × 24 phase encodings.

The GS model for water removal was formulated in the spectral domain, because the separation of water and metabolite signals is based primarily on their distinct spectral locations (i.e., water resonates at about 4.7 ppm, and most detectable metabolites resonate between 0.8 and 4.3 ppm). The spectral GS model effectively absorbed the frequency information of the water reference; the modulation function, $\sum_{n=-N_w}^{N_w} \beta_n\left(\boldsymbol{x},\theta\right)e^{-i2\pi n\Delta f t}$, was used to capture the interscan water signal changes due to field variations, which can be modeled as a linear combination of frequency components within a certain range $[-N_W\Delta f, N_W\Delta f]$[37] as follows:

$$s_W\left(\boldsymbol{x},t,\theta\right) \approx \sum_{n=-N_W}^{N_W} \beta_n\left(\boldsymbol{x},\theta\right)e^{-i2\pi n\Delta f t}, \tag{3}$$

leading to the proposed GS model. In practice, the field varies over a small range, resulting in a small model order and a few DOFs (typically $N_W = 4$). Besides, it is well known that spatial variations in field drift are rather smooth.[38] The small DOF of the proposed spectral model and the smooth nature of the model coefficients make it feasible to reconstruct and remove water signals from limited k-space data.

With the proposed GS model in Eq. (1), estimation of lipid and water signals from the low-resolution data sets was done by solving the following linear least-squares problem:

$$\left\{\widehat{\boldsymbol{\alpha}}\left(\theta\right),\widehat{\boldsymbol{\beta}}\left(\theta\right)\right\} = \arg\min_{\{\boldsymbol{\alpha}(\theta),\boldsymbol{\beta}(\theta)\}} \left\|\mathbf{d}(\theta) - \boldsymbol{\Omega}(\theta)\mathcal{F}(\mathbf{G}_L\boldsymbol{\alpha}_L(\theta) + \mathbf{G}_W\boldsymbol{\beta}_W(\theta))\right\|_2^2, \tag{4}$$

where $\mathbf{d}(\theta)$ is the data vector acquired with flip angle θ; $\boldsymbol{\Omega}(\theta)$ is the corresponding (k,t)-space sampling operator; $\mathcal{F}$ the Fourier encoding operator; $\mathbf{G}_L$ is the GS encoding operator for lipid signals; $\mathbf{G}_W$ is the GS encoding operator for water signals (i.e., matrices whose N_L or N_W columns contain frequency-modulated reference images); $\boldsymbol{\alpha}(\theta)$ is the vector of lipid GS coefficients; and $\boldsymbol{\beta}(\theta)$ is the vector of water GS coefficients. The estimated lipid and water signals, $\mathbf{G}_L\hat{\boldsymbol{\alpha}}(\theta)$ and $\mathbf{G}_W\hat{\boldsymbol{\beta}}\left(\theta\right)$, were then removed from the measured (k,t)-space data.

2.2.2 | Spatiospectral reconstruction of metabolite signals: For reconstruction of metabolite signals, the basic SPICE method used a subspace approach to handle the large measurement noise. Particularly, a subspace model was adopted to exploit the spatiospectral correlations of MRSI signals (known as partial separability[15]) for effective denoising.[20] In this work, we extended the union-of-subspaces model to a union-of-low-rank-tensors model for representing the VFA metabolite signals[15,30,39,40]:

$$\rho\left(\boldsymbol{x}, f, \theta\right) = \sum_{m=1}^{M} \rho_m\left(\boldsymbol{x}, f, \theta\right) = \sum_{m=1}^{M}\left[\sum_{p=1}^{P_m}\sum_{q=1}^{Q_m}\sum_{r=1}^{R_m} t_{m,p,q,r}\ u_{m,p}(\boldsymbol{x})v_{m,q}(f)w_{m,r}(\theta)\right], \tag{5}$$

where $\rho_m(\boldsymbol{x}, f, \theta)$ is the signal from the m^{th} molecule; $t_{m,p,q,r}$ is the core tensor; $v_{m,q}(f)$ are the spectral basis functions; $w_{m,r}(\theta)$ are the T_1-weighting basis functions; and $u_{m,p}(\boldsymbol{x})$ are the spatial coefficients, respectively. This model includes major brain metabolites, like NAA, Cr, Cho and myo-inositol (mI), as well as macromolecules. Other molecules, like glutamate, glutamine, gamma-aminobutyric acid and lactate, can also be incorporated in the model. In this study, we did not include them, as they have much lower SNR and larger spectral overlapping to permit reliable T_1 estimates using the proposed fast data-acquisition scheme at 3 T. One key advantage of this model is the significant reduction in the DOF. For example, with the conventional Fourier model, the DOF of an image of 80 × 80 × 24 spatial matrix size, 512 spectral points, and five flip angles is 393 million. With the LRT model, the DOF is about 6 million (50-fold reduction). The reduced DOF enables the reconstruction of high-quality images from undersampled and noisy data.

The LRT model in Eq. (5) also decouples signal variations along spatial, spectral, and flip-angle dimensions, enabling effective incorporation of physics-based prior information in the form of prelearned basis functions. In this work, we prelearned both spectral and flip-angle basis functions to facilitate the reconstruction of $\rho(\boldsymbol{x}, f, \theta)$. The spectral basis functions for each molecule were obtained by integrating quantum mechanical simulation with empirical spectral parameter distributions from training data.[20,41] Specifically, the following parametric model was used to represent spectral signals:

$$s_m(f) = \int_{-\infty}^{\infty}\left[c_m\ \phi_m(t)e^{-t/T_{2,m}^{*}}\ e^{-i2\pi\Delta f_m t}\ h(t)\right]e^{-i2\pi f t}\mathrm{d}t, \tag{6}$$

where c_m is the concentration of the mth molecule; $\phi_m(t)$ the resonance structure function determined by quantum simulation; and $\left(T_{2,m}^{*}, \Delta f_m, h(t)\right)$ is a set of spectral parameters for Lorentzian linewidth, frequency shift, and lineshape variations,[20] respectively. A set of model parameters was estimated by fitting the spectral signal model in Eq. (6) to training data acquired from healthy subjects, then a Casorati matrix was generated with columns containing the spectral signals synthesized using the fitted parameters. Finally, the basis functions $\hat{v}_{m,q}(f)$ were estimated by performing singular value decomposition on the Casorati matrix.

Similarly, the Casorati matrix for estimating T_1-weighting basis functions was generated using the following steady-state signal model[42,43]:

$$f_m(\theta) = a_m \frac{1 - \exp(-\mathrm{TR}/T_{1,m})}{1 - \cos(B_1^+\theta)\exp(-\mathrm{TR}/T_{1,m})} \sin(B_1^+\theta), \tag{7}$$

where a_m is the proton density of the mth molecule; $T_{1,m}$ is the T_1 value; and B_1^+ is the $B_1{}^+$ inhomogeneity. A set of feasible molecular T_1 values (300–1800 ms, covering typical T_1 ranges of metabolites and macromolecules) and $B_1{}^+$ inhomogeneities (0.5–1.5, covering typical $B_1{}^+$ values at 3 T[43,44]) were used to synthesize T_1-weighting functions, filling the columns of the Casorati matrix, from which we derived the T_1-weighting basis functions $\widehat{w}_{m,r}(\theta)$.

With the prelearned basis functions, the reconstruction problem was simplified to the estimation of core tensor $t_{m,p,q,r}$ and spatial coefficients $u_{m,p}(\boldsymbol{x})$. We estimated them by solving the following optimization problem that enforces data consistency and edge-preserving regularization on the spatial coefficients:

$$\min_{\{t_{m,p,q,r},\mathbf{u}_{m,p}\}} \left\| \mathbf{d}_{\mathrm{r}} - \boldsymbol{\Omega}\mathscr{F}\mathbf{B}\left(\sum_{m=1}^{M} \left(\sum_{p=1}^{P_m} \sum_{q=1}^{Q_m} \sum_{r=1}^{R_m} t_{m,p,q,r}\ \mathbf{u}_{m,p} \circ \widehat{\mathbf{v}}_{m,q} \circ \widehat{\mathbf{w}}_{m,r} \right) \right) \right\|_2^2 + \lambda \sum_{m=1}^{M} \sum_{p=1}^{P_m} \|\mathbf{W}\mathbf{u}_{m,p}\|_2^2, \tag{8}$$

where $\mathbf{d}_{\mathrm{r}}$ is the vector representing nuisance-removed $(\boldsymbol{k}, t, \theta)$-space data; $\boldsymbol{\Omega}$ is the sampling operator in $(\boldsymbol{k}, t, \theta)$-space; $\mathbf{B}$ is the B_0 inhomogeneity effect operator; $\mathbf{u}_{m,p}$, $\widehat{\mathbf{v}}_{m,q}$, and $\widehat{\mathbf{w}}_{m,r}$ are the vectors for spatial coefficients, prelearned spectral basis and T_1-weighting basis, respectively; "$\circ$" is the vector outer product operator; λ are the regularization parameters (selected according to the discrepancy principle[45]); and $\mathbf{W}$ is the edge-preserving spatial regularization matrix.[46] The detailed algorithm to solve Eq. (8) is described in the Supporting Information. After the core tensor $\hat{t}_{m,p,q,r}$ and spatial coefficients $\hat{u}_{m,p}(\boldsymbol{x})$ were determined, the metabolite signals were synthesized based on Eq. (5). The final T_1 maps were calculated by fitting the steady-state signal model in Eq. (7) using the variable projection algorithm.[47]

3 | METHODS

3.1 | Acquisition of phantom data

We used a uniform MRS phantom (SPECTER phantom; Gold Standard Phantoms LTD; NAA 12.5 mM, Cr 10.0 mM, Cho 3.0 mM, mI 7.5 mM, glutamate 12.5 mM, lactate 5.0 mM, gamma-aminobutyric acid 2.0 mM) to validate the proposed method. The phantom experiment was carried out on a 3T scanner (MAGNETOM Prisma; Siemens Healthcare, Erlangen, Germany) equipped with a 20-channel head coil. A VFA SPICE data set was acquired with the following parameters: FOV = 240 × 240 × 72 mm^3, matrix size = 78 × 122 × 24, TR/TE = 160/1.6 ms, flip angle = 17°/22°/27°/32°/37°, echo space = 1.76 ms, readout bandwidth = 167 kHz, and scan time = 14:26 min.

3.2 | Acquisition of in vivo data

The in vivo study was approved by the local institutional review board. Five healthy subjects were scanned using the same VFA SPICE sequence as used in the phantom experiment. One subject was scanned once to show the feasibility of the proposed method, and the other four were scanned twice in test–retest sessions separated by at least 14 days to evaluate the reproducibility. The protocol also includes an MPRAGE scan with the following parameters: FOV = 240 × 240 × 192 mm^3, spatial resolution = 1.0 × 1.0 × 1.0 mm^3, TR/TE/TI = 1900/2.29/900 ms, flip angle = 9°, and scan time = 5:07 min.

3.3 | Data processing and analysis

The MPRAGE data were used as anatomical reference images to derive spatial supports for nuisance removal and edge weights for metabolite signal reconstruction. Gray-matter and white-matter masks were obtained using the *Statistical Parametric Mapping* toolbox (SPM12; http://www.fil.ion.ucl.ac.uk/spm/) for the estimation of B_1 fields from water signals.

Main field drifts (global frequency drifts) and spatial misalignment (modeled as rigid-body transformations) among VFA MRSI data sets were estimated from water signals and corrected on the entire data set. Nuisance signals were then estimated from the high-resolution data acquired with Ernst-angle excitation, serving as reference images for nuisance removal from low-resolution data. The high-resolution data also provided sensitivity maps for coil combination and B_0 maps for metabolite signal reconstruction.[48,49] B_1^+ and $B1^-$ maps were estimated from the VFA unsuppressed water signals using a polynomial fitting method.[43] The B_1^+ map was incorporated into the metabolite T_1 fitting model in Eq. (7), and the B_1^- map was corrected from the fitted metabolite concentration maps.

In phantom data analysis, Cho was used as the reference to normalize metabolite concentrations, and the T_1-corrected concentrations of other metabolites were compared with the ground-truth values. In human data analysis, the reproducibility of metabolite T_1 values in test–retest experiments were evaluated in gray-matter and white-matter regions of four brain lobes (frontal/parietal/temporal/occipital) using Bland–Altman analysis.[50] Paired *t*-tests were used to compare the regional T_1 values between test and retest experiments.

4 | RESULTS

Figure 2 shows the VFA SPICE results obtained from the uniform phantom. Figure 2A shows the B_1^+ and B_1^- maps derived from the unsuppressed water signals. The metabolite concentration and T_1 maps before and after B_1 correction are displayed in Figure 2B. The proposed method produced uniform concentration and T_1 maps, as supported by the histograms of metabolite T_1 values in Figure S1. The correction of T_1-weighting effects in metabolite concentrations resulted in a noticeable reduction in relative errors with respect to the ground truth, as shown in Figure 2C (NAA: 16.8%–1.6%, Cr: 4.1%–0.4%, mI: 2.3%–0.9%).

Experimental VFA SPICE results obtained from a healthy subject are presented in Figures 3–5. Figure 3 displays the results obtained from the unsuppressed water signals. From the reconstructed VFA water images (shown in Figure S2), high-quality B_1^+ and B_1^- maps were estimated,[43] which were subsequently used for corrections in the T_1 maps of both water and metabolites. Water T_1 maps are shown in Figure 3, which exhibited noticeable improvements in spatial homogeneity after the correction of B_1^+ effects. Figure 4 shows the reconstructed VFA MRSI data, including VFA metabolite images in Figure 4A and localized spectra in Figure 4B. The metabolite images demonstrated high-quality reconstruction with high SNR and clear gray-matter/white-matter contrast. The signal evolution with the changes of flip angles was also noticeable in both metabolite maps and localized spectra, with the highest signal intensity at the Ernst-angle frame. Figure 5A presents the resulting metabolite T_1 maps estimated from the VFA metabolite images. These 3D metabolite T_1 maps have extensive brain coverage and excellent SNR. The T_1 curves and their fitting results from two representative spatial voxels are shown in Figure 5B. All four metabolites have excellent fitting with negligible residue.

Figure 6 shows the reproducibility results. Figure 6A displays the metabolite T_1 maps obtained from test and retest experiments for 2 subjects. Their regional metabolite and water T_1 values are provided in Table 1. The maps from the third and the fourth subjects are shown in Figure S3. All subjects yielded high-quality and consistent metabolite T_1 maps. Bland–Altman reproducibility analysis was performed, as shown in Figure 6B. The reproducibility coefficients for NAA, Cr, Cho, and mI T_1 values were 7.8%, 9.0%, 10.5% and 10.7%, respectively. For all the metabolites, the mean differences of T_1 values in two measurements were close to zero, and the 95% agreement lines of differences were very small compared with the mean values. These results demonstrated no significant bias between the repetitions ($p > 0.05$ for all metabolites), and the variations were within a reasonable range.

5 | DISCUSSION

This work introduces VFA SPICE for 3D metabolite T_1 mapping within a practically feasible scan time. The results obtained from phantom experiments, in vivo feasibility assessments, and in vivo reproducibility studies demonstrated its accuracy and reliability in measuring metabolite T_1 values in a scan of 14.5 min. It would take about 6 h for the state-of-the-art single-slice metabolite T_1 mapping methods to achieve the same spatial coverage.[13] This fast-imaging capability results from an innovative extension of basic SPICE data acquisition with VFA signal excitation and variable-density data sampling. In data processing, the challenges of removing nuisance signals from limited k-space data were addressed using high-resolution reference data through a novel GS model-based algorithm; metabolite image reconstruction from undersampled noisy data was solved using an LRT model with prelearned basis functions.

This study presents the first 3D mapping of metabolite T_1 values with near whole-brain coverage. Compared with currently available metabolite T_1 mapping methods with only single-voxel or single-slice coverage, the extended spatial coverage of VFA SPICE provided two major benefits. First, volumetric imaging reduced the variations in the measurement due to voxel/slice placement, which could be subjective and susceptible to errors of the

operators. Second, metabolite T_1 values in multiple brain regions can be simultaneously measured and systematically compared, instead of repeating the measurement for different regions. The quantitative values given in Table 1 were in good agreement with previous reports from single-voxel MRS studies,[5–7,9] as summarized in Table S1. The relative metabolite T_1 differences compared with most prior studies are within 5%.

The correction of T_1 relaxation effects in short-TR MRSI data like basic SPICE is needed for accurate metabolite quantification. Due to the difficulty in obtaining 3D metabolite T_1 maps for each individual, conventional T_1 correction approaches rely on either surrogate water T_1 values or tissue-based literature metabolite T_1 values.[51–55] However, tissue-based literature-value T_1 correction may introduce inaccuracies due to spatial-dependent and subject-dependent variations (Figures 5 and 6) and would fail in pathological conditions. Water T_1 maps, on the other hand, do not accurately represent metabolite T_1 values (Figure 3 and Table 1). This work provides molecule-specific T_1 values from each individual for effective T_1 correction. Additionally, the unsuppressed VFA water signals allow for the estimation of B_1^+ and B_1^- maps, which are also desired for quantitative imaging. Overall, the proposed method enables effective correction of T_1 saturation and B_1 inhomogeneities effects in SPICE data.

Further refinement and improvement can be made to the proposed method to enhance its performance and practical utility. First, ultrahigh-field MR systems could provide higher SNR and better spectral separation,[56,57] enabling T_1 mapping for a greater range of molecules. Second, only a small number of subjects were recruited in this feasibility study. As more metabolite T_1 mapping data sets become available, machine learning methods can be applied to derive stronger data-driven priors (e.g., distributions of metabolite T_1 values) for further acceleration. Third, the flip-angle values were selected to be uniformly distributed. These values can be further optimized, such as through Cramer-Rao lower bound analysis.[58] Finally, the data processing takes a relatively long time (~8 h on a workstation with a 24-core central processor operating at 2.6 GHz) and a large amount of memory (~50 GB). Optimizing the algorithm implementation and exploring the possibility of online reconstruction on the scanner would be desirable for practical applications.

6 | CONCLUSION

This paper demonstrated the feasibility of accelerated 3D metabolite T_1 mapping using VFA SPICE. The proposed method has been evaluated using phantom and healthy volunteer data, resulting in high-quality and reproducible metabolite T_1 maps. The proposed method shows promise as a useful tool for mapping metabolite T_1 distributions and correcting T_1 effects in short-TR MRSI data.

Supplementary Material

Refer to Web version on PubMed Central for supplementary material.

ACKNOWLEDGMENTS

This work was supported by the National Institutes of Health, grant number: P41EB022544, R01EB033582.

Funding information

National Institutes of Health, Grant/Award Numbers: P41EB022544, R01EB033582

DATA AVAILABILITY STATEMENT

The code and data that support the findings of this study are available from the corresponding author, upon reasonable request.

REFERENCES

1. Peng X, Lam F, Li Y, Clifford B, Liang Z-P. Simultaneous QSM and metabolic imaging of the brain using SPICE. Magn Reson Med. 2018;79:13–21. doi:10.1002/mrm.26972 [PubMed: 29067730]
2. Bogner W, Otazo R, Henning A. Accelerated MR spectroscopic imaging—a review of current and emerging techniques. NMR Biomed. 2021;34:e4314. doi:10.1002/nbm.4314 [PubMed: 32399974]
3. Moser P, Eckstein K, Hingerl L, et al. Intra-session and inter-subject variability of 3D-FID-MRSI using single-echo volumetric EPI navigators at 3T. Magn Reson Med. 2020;83:1920–1929. doi:10.1002/mrm.28076 [PubMed: 31721294]
4. Knight-Scott J, Brennan P, Palasis S, Zhong X. Effect of repetition time on metabolite quantification in the human brain in 1H MR spectroscopy at 3 Tesla. J Magn Reson Imaging. 2017;45:710–721. doi:10.1002/jmri.25403 [PubMed: 27474158]
5. Mlynárik V, Gruber S, Moser E. Proton T1 and T2 relaxation times of human brain metabolites at 3 Tesla. NMR Biomed. 2001;14:325–331. doi:10.1002/nbm.713 [PubMed: 11477653]
6. Li Y, Xu D, Ozturk-Isik E, et al. T1 and T2 metabolite relaxation times in normal brain at 3T and 7T. J Mol Imaging Dyn. 2013;S1:002. doi:10.4172/2155-9937.S1-002
7. An L, Li S, Shen J. Simultaneous determination of metabolite concentrations, T1 and T2 relaxation times. Magn Reson Med. 2017;78:2072–2081. doi:10.1002/mrm.26612 [PubMed: 28164364]
8. An L, Araneta MF, Victorino M, Shen J. Determination of brain metabolite T1 without interference from macromolecule relaxation. J Magn Reson Imaging. 2020;52:1352–1359. doi:10.1002/jmri.27259 [PubMed: 32618104]
9. Ethofer T, Mader I, Seeger U, et al. Comparison of longitudinal metabolite relaxation times in different regions of the human brain at 1.5 and 3 Tesla. Magn Reson Med. 2003;50:1296–1301. doi:10.1002/mrm.10640 [PubMed: 14648578]
10. Li Y, Srinivasan R, Ratiney H, Lu Y, Chang SM, Nelson SJ. Comparison of T1 and T2 metabolite relaxation times in glioma and normal brain at 3T. J Magn Reson Imaging. 2008;28:342–350. doi:10.1002/jmri.21453 [PubMed: 18666155]
11. Brief EE, Vavasour IM, Laule C, Li DKB, MacKay AL. Proton MRS of large multiple sclerosis lesions reveals subtle changes in metabolite T1 and area. NMR Biomed. 2010;23:1033–1037. doi:10.1002/nbm.1527 [PubMed: 20963799]
12. Ratiney H, Noworolski SM, Sdika M, et al. Estimation of metabolite T1 relaxation times using tissue specific analysis, signal averaging and bootstrapping from magnetic resonance spectroscopic imaging data. MAGMA. 2007;20:143–155. doi:10.1007/s10334-007-0076-0 [PubMed: 17602253]
13. Klauser A, Grouiller F, Courvoisier S, Lazeyras F. High-resolution T1 maps of brain metabolites. Proceedings of the 27th Annual Meeting of ISMRM; 2019:2488.
14. Ma C, Han P, Fakhri G. Simultaneous mapping of metabolite concentration and T1 relaxation time using subspace imaging accelerated inversion recovery MRSI. Proceedings of the 29th Annual Meeting of ISMRM [Virtual]; 2021:3050.
15. Liang Z-P. Spatiotemporal imaging with partially separable functions. Proceedings of the 4th IEEE International Symposium on Biomedical Imaging; 2007:988–991. doi:10.1109/ISBI.2007.357020
16. Lam F, Liang Z-P. A subspace approach to high-resolution spectroscopic imaging. Magn Reson Med. 2014;71:1349–1357. doi:10.1002/mrm.25168 [PubMed: 24496655]
17. Lam F, Ma C, Clifford B, Johnson CL, Liang Z-P. High-resolution 1H-MRSI of the brain using SPICE: data acquisition and image reconstruction. Magn Reson Med. 2016;76:1059–1070. doi:10.1002/mrm.26019 [PubMed: 26509928]

18. Ma C, Lam F, Ning Q, Johnson CL, Liang Z-P. High-resolution 1H-MRSI of the brain using short-TE SPICE. Magn Reson Med. 2017;77:467–479. doi:10.1002/mrm.26130 [PubMed: 26841000]
19. Guo R, Zhao Y, Li Y, Li Y, Liang Z-P. Simultaneous metabolic and functional imaging of the brain using SPICE. Magn Reson Med. 2019;82:1993–2002. doi:10.1002/mrm.27865 [PubMed: 31294487]
20. Lam F, Li Y, Guo R, Clifford B, Liang ZP. Ultrafast magnetic resonance spectroscopic imaging using SPICE with learned subspaces. Magn Reson Med. 2020;83:377–390. doi:10.1002/mrm.27980 [PubMed: 31483526]
21. Guo R, Zhao Y, Li Y, et al. Simultaneous QSM and metabolic imaging of the brain using SPICE: further improvements in data acquisition and processing. Magn Reson Med. 2021;85:970–977. doi:10.1002/mrm.28459 [PubMed: 32810319]
22. Posse S, Tedeschi G, Risinger R, Ogg R, Le BD. High speed 1H spectroscopic imaging in human brain by echo planar spatial-spectral encoding. Magn Reson Med. 1995;33:34–40. doi:10.1002/mrm.1910330106 [PubMed: 7891533]
23. Li Y, Wang T, Zhang T, et al. Fast high-resolution metabolic imaging of acute stroke with 3D magnetic resonance spectroscopy. Brain. 2021;143:3225–3233. doi:10.1093/BRAIN/AWAA264
24. Lin Z, Meng Z, Wang T, et al. Predicting the onset of ischemic stroke with fast high-resolution 3D MR spectroscopic imaging. J Magn Reson Imaging. 2023;58:838–847. doi:10.1002/jmri.28596 [PubMed: 36625533]
25. Meng Z, Guo R, Wang T, et al. Prediction of stroke onset time with combined fast high-resolution magnetic resonance spectroscopic and quantitative T2 mapping. IEEE Trans Biomed Eng. 2023;70:3147–3155. doi:10.1109/TBME.2023.3277546 [PubMed: 37200119]
26. Guo R, Ma C, Li Y, et al. High-resolution label-free molecular imaging of brain tumor. Proceedings of the 43rd Annual International Conference of the IEEE Engineering in Medicine & Biology Society (EMBC); 2021:3049–3052. doi:10.1109/EMBC46164.2021.9630623
27. Hu J, Zhang M, Guo R, et al. Fast 3D high-resolution metabolic imaging in Alzheimer's disease using SPICE. Proceedings of the Annual Meeting of ISMRM [Virtual]; 2020:215.
28. Huang H, Zhang M, Guo R, et al. Simultaneous 18F-FDG-PET and 1H-MRSI metabolic imaging in epilepsy patients: a feasibility study. Proceedings of the Annual Meeting of ISMRM [Virtual]; 2020:929.
29. Stikov N, Boudreau M, Levesque IR, Tardif CL, Barral JK, Pike GB. On the accuracy of T1 mapping: searching for common ground. Magn Reson Med. 2015;73:514–522. doi:10.1002/mrm.25135 [PubMed: 24578189]
30. Ma C, Lam F, Johnson CL, Liang Z-P. Removal of nuisance signals from limited and sparse 1H MRSI data using a union-of-subspaces model. Magn Reson Med. 2016;75:488–497. doi:10.1002/mrm.25635 [PubMed: 25762370]
31. Liang Z-P, Lauterbur PC. A generalized series approach to MR spectroscopic imaging. IEEE Trans Med Imaging. 1991;10:132–137. doi:10.1109/42.79470 [PubMed: 18222809]
32. Hess CP, Liang Z-P, Lauterbur PC. Maximum cross-entropy generalized series reconstruction. Int J Imaging Syst Technol. 1999;10:258–265. doi:10.1002/(SICI)1098-1098(1999)10:3<258::AID-IMA6>3.0.CO;2-7
33. Mohan S, Verma A, Lim CCT, Hui F, Kumar S. Lipid resonance on in vivo proton MR spectroscopy: value of other metabolites in differential diagnosis. Neuroradiol J. 2010;23:269–278. doi:10.1177/197140091002300302 [PubMed: 24148583]
34. Narayana PA. Magnetic resonance spectroscopy in the monitoring of multiple sclerosis. J Neuroimaging. 2005;15:46S–57S. doi:10.1177/1051228405284200 [PubMed: 16385018]
35. Delikatny EJ, Chawla S, Leung D, Poptani H. MR-visible lipids and the tumor microenvironment. NMR Biomed. 2011;24:592–611. doi:10.1002/nbm.1661 [PubMed: 21538631]
36. Liang Z-P, Lauterbur PC. Principles of Magnetic Resonance Imaging: A Signal Processing Perspective. SPIE Optical Engineering Press; 2000.
37. Li Y, Xiong J, Guo R, Zhao Y, Li Y, Liang Z-P. Improved estimation of myelin water fractions with learned parameter distributions. Magn Reson Med. 2021;86:2795–2809. doi:10.1002/mrm.28889 [PubMed: 34216050]

38. Hui SCN, Mikkelsen M, Zöllner HJ, et al. Frequency drift in MR spectroscopy at 3T. Neuroimage. 2021;241:118430. doi:10.1016/j.neuroimage.2021.118430 [PubMed: 34314848]
39. He J, Liu Q, Christodoulou AG, Ma C, Lam F, Liang Z-P. Accelerated high-dimensional MR imaging with sparse sampling using low-rank tensors. IEEE Trans Med Imaging. 2016;35:2119–2129. doi:10.1109/TMI.2016.2550204 [PubMed: 27093543]
40. Zhao Y, Guo R, Li Y, et al. 3D high-resolution T1 mapping of brain metabolites. Proceedings of the 32nd Annual Meeting of ISMRM; 2023:3693.
41. Li Y, Lam F, Clifford B, Liang Z-P. A subspace approach to spectral quantification for MR spectroscopic imaging. IEEE Trans Biomed Eng. 2017;64:2486–2489. doi:10.1109/TBME.2017.2741922 [PubMed: 28829303]
42. Zhao B, Lu W, Hitchens TK, Lam F, Ho C, Liang Z-P. Accelerated MR parameter mapping with low-rank and sparsity constraints. Magn Reson Med. 2015;74:489–498. doi:10.1002/mrm.25421 [PubMed: 25163720]
43. Wang YY, Chen Y, Wu D, et al. STrategically acquired gradient Echo (STAGE) imaging, part II: correcting for RF inhomogeneities in estimating T1 and proton density. Magn Reson Imaging. 2018;46:140–150. doi:10.1016/j.mri.2017.10.006 [PubMed: 29061370]
44. Zhang T, Zhao Y, Jin W, et al. B1 mapping using pre-learned subspaces for quantitative brain imaging. Magn Reson Med. 2023;90:1–13. doi:10.1002/mrm.29764
45. Vogel CR. Computational Methods for Inverse Problems. Society for Industrial and Applied Mathematics; 2002.
46. Haldar JP, Hernando D, Song S-K, Liang Z-P. Anatomically constrained reconstruction from noisy data. Magn Reson Med. 2008;59:810–818. doi:10.1002/mrm.21536 [PubMed: 18383297]
47. Golub G, Pereyra V. Separable nonlinear least squares: the variable projection method and its applications. Inverse Probl. 2003;19:R1–R26. doi:10.1088/0266-5611/19/2/201
48. Natt O, Bezkorovaynyy V, Michaelis T, Frahm J. Use of phased array coils for a determination of absolute metabolite concentrations. Magn Reson Med. 2005;53:3–8. doi:10.1002/mrm.20337 [PubMed: 15690495]
49. Peng X, Nguyen H, Haldar J, Hernando D, Wang X-P, Liang Z-P. Correction of field inhomogeneity effects on limited k-space MRSI data using anatomical constraints. Proceedings of the Annual International Conference of the IEEE Engineering in Medicine and Biology; 2010:883–886. doi:10.1109/IEMBS.2010.5627873
50. Altman DG, Bland JM. Measurement in medicine: the analysis of method comparison studies. Stat. 1983;32:307. doi:10.2307/2987937
51. Bonekamp D, Smith MA, Zhu H, Barker PB. Quantitative SENSE-MRSI of the human brain. Magn Reson Imaging. 2010;28:305–313. doi:10.1016/j.mri.2009.11.003 [PubMed: 20045600]
52. Wright AM, Murali-Manohar S, Henning A. Quantitative T1-relaxation corrected metabolite mapping of 12 metabolites in the human brain at 9.4 T. Neuroimage. 2022;263:119574. doi:10.1016/j.neuroimage.2022.119574 [PubMed: 36058442]
53. Gasparovic C, Song T, Devier D, et al. Use of tissue water as a concentration reference for proton spectroscopic imaging. Magn Reson Med. 2006;55:1219–1226. doi:10.1002/mrm.20901 [PubMed: 16688703]
54. Bogner W, Gruber S, Trattnig S, Chmelik M. High-resolution mapping of human brain metabolites by free induction decay 1H MRSI at 7 T. NMR Biomed. 2012;25:873–882. doi:10.1002/nbm.1805 [PubMed: 22190245]
55. Hangel G, Spurny-Dworak B, Lazen P, et al. Inter-subject stability and regional concentration estimates of 3D-FID-MRSI in the human brain at 7 T. NMR Biomed. 2021;34:e4596. doi:10.1002/nbm.4596 [PubMed: 34382280]
56. De Graaf RA. In Vivo NMR Spectroscopy: Principles and Techniques. John Wiley & Sons; 2007.
57. Henning A. Proton and multinuclear magnetic resonance spectroscopy in the human brain at ultra-high field strength: a review. Neuroimage. 2018;168:181–198. doi:10.1016/j.neuroimage.2017.07.017 [PubMed: 28712992]
58. Belsley G, Tyler DJ, Robson MD, Tunnicliffe EM. Optimal flip angles for in vivo liver 3D T1 mapping and B1+ mapping at 3T. Magn Reson Med. 2023;90:950–962. doi:10.1002/mrm.29683 [PubMed: 37125661]

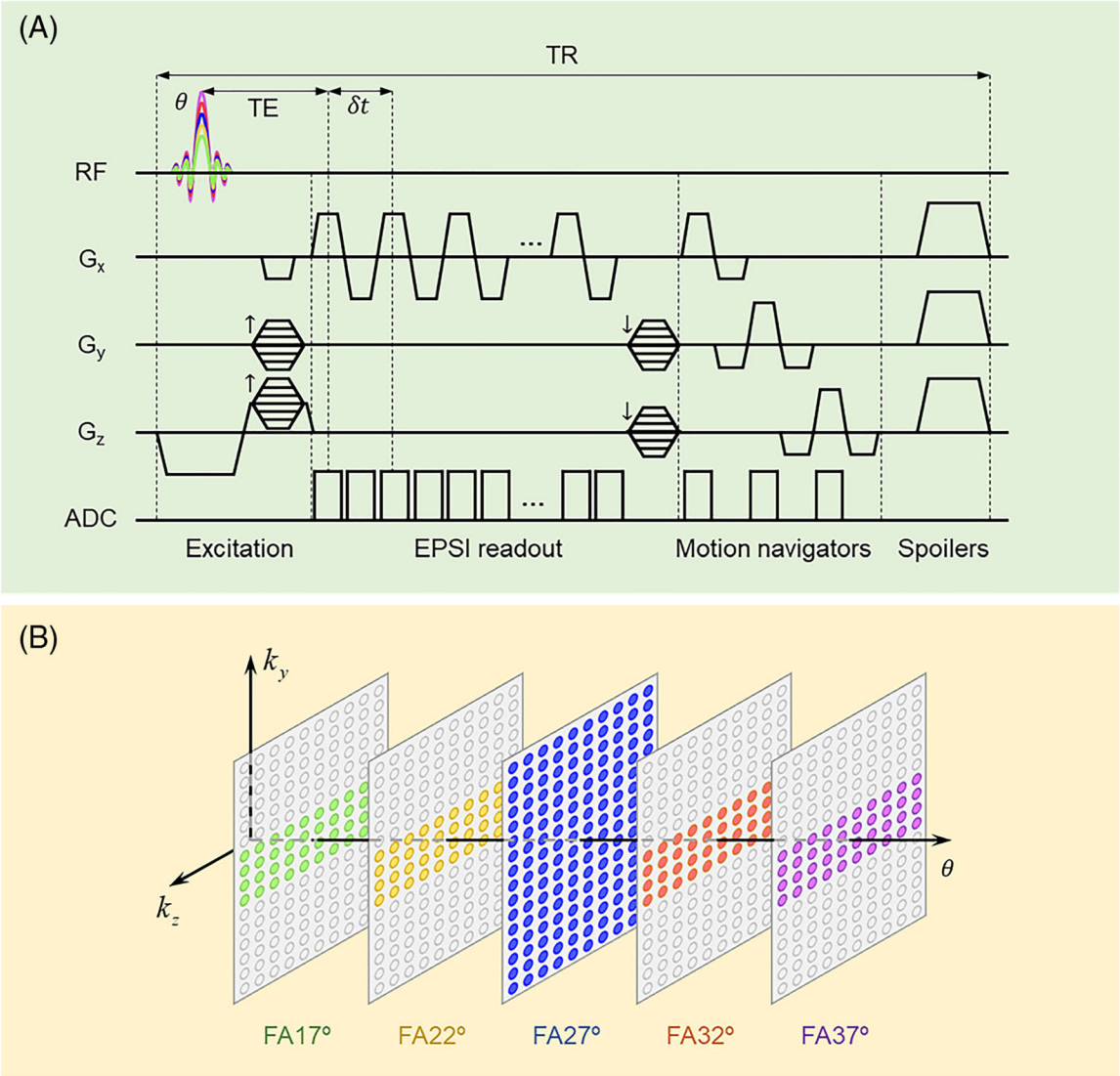

FIGURE 1.

Illustration of the proposed data-acquisition scheme for accelerated 3D metabolite T_1 mapping. (A) The variable-flip-angle (VFA) FID MRSI pulse sequence with extended echo-planar spectroscopic imaging (EPSI) readouts and motion navigators. (B) The sampling strategy for the high-dimensional data space. Extended k-space was covered in the Ernst-angle excitations (flip angle [FA] = 27°), whereas other data were sampled with limited k-space coverage.

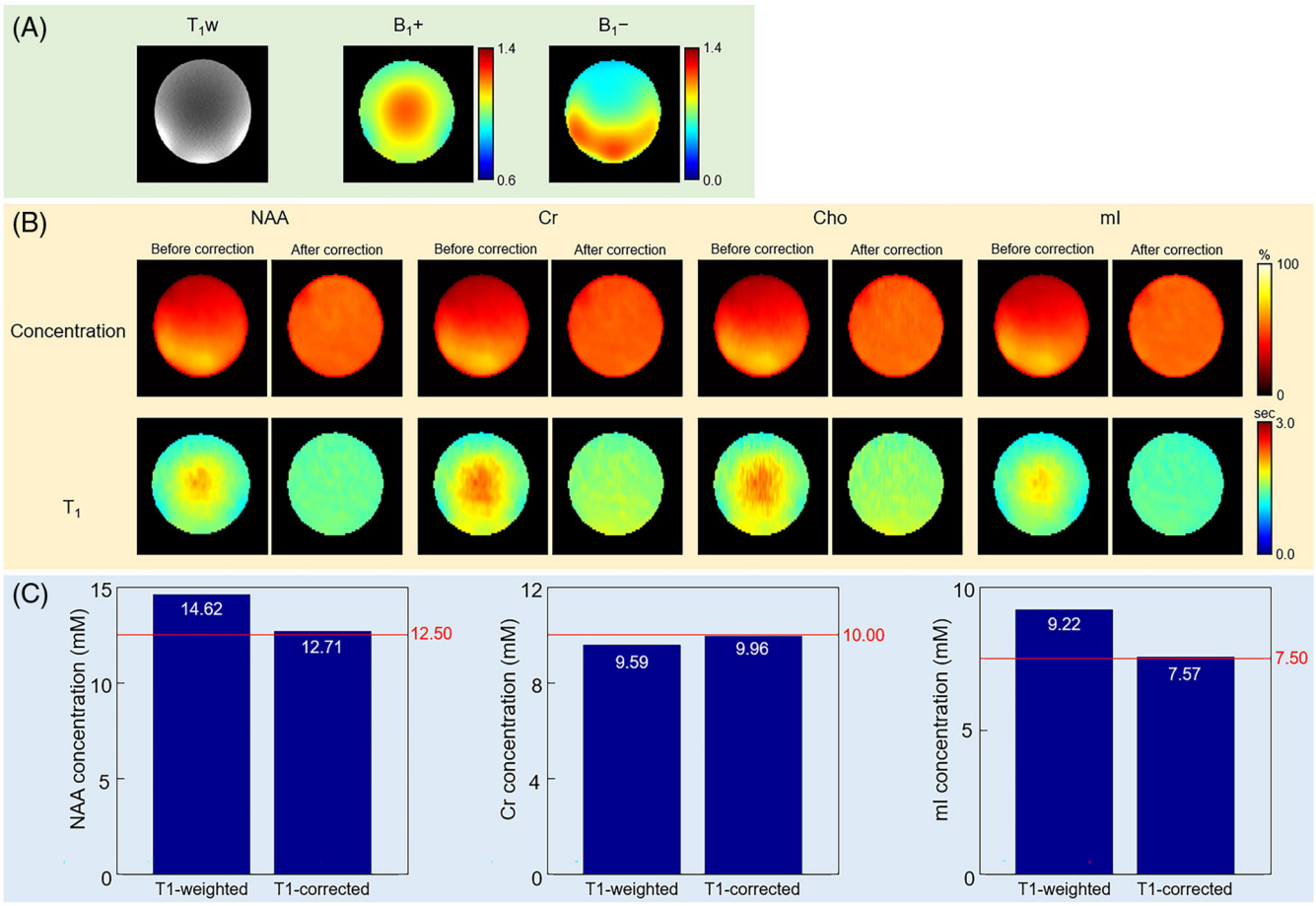

FIGURE 2.

Phantom experiment results. (A) T_1-weighted structural image and the B_1 maps estimated from unsuppressed water MRSI signals. (B) Concentration and T_1 maps of N-acetylaspartate (NAA), creatine (Cr), choline (Cho) and myo-inositol (mI) before and after B_1 corrections. Both metabolite concentration and T_1 maps became more homogeneous after corrections. (C) Metabolite concentrations measured in the phantom, using Cho concentration (3.00 mM) for normalization. T_1-weighted concentrations were obtained from the Ernst-angle excitation data, and T_1-corrected concentrations were obtained by fitting the variable-flip-angle data. With T_1 weighting effects corrected, the concentrations of NAA, Cr, and mI become closer to the ground-truth concentrations (*red lines*).

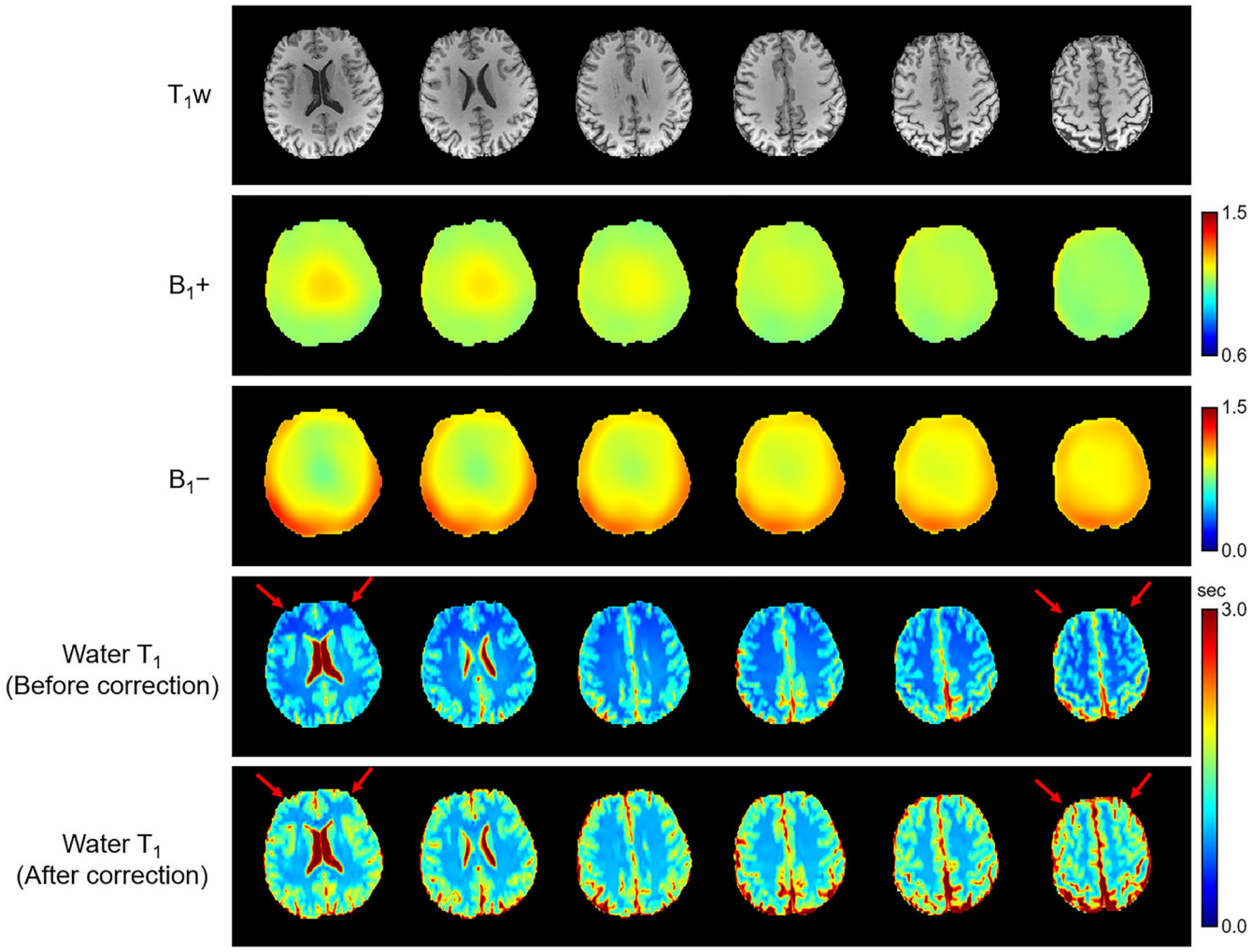

FIGURE 3.

T_1-weighted (T1w) anatomical image, B_1 maps, and water T_1 maps (before and after B_1 corrections) obtained from a healthy subject. B_1 maps and water T_1 maps were derived from the unsuppressed water signals in MRSI data. Noticeable improvement in spatial homogeneity of water T_1 maps was observed after the correction of B_1^+ effects (*red arrows*).

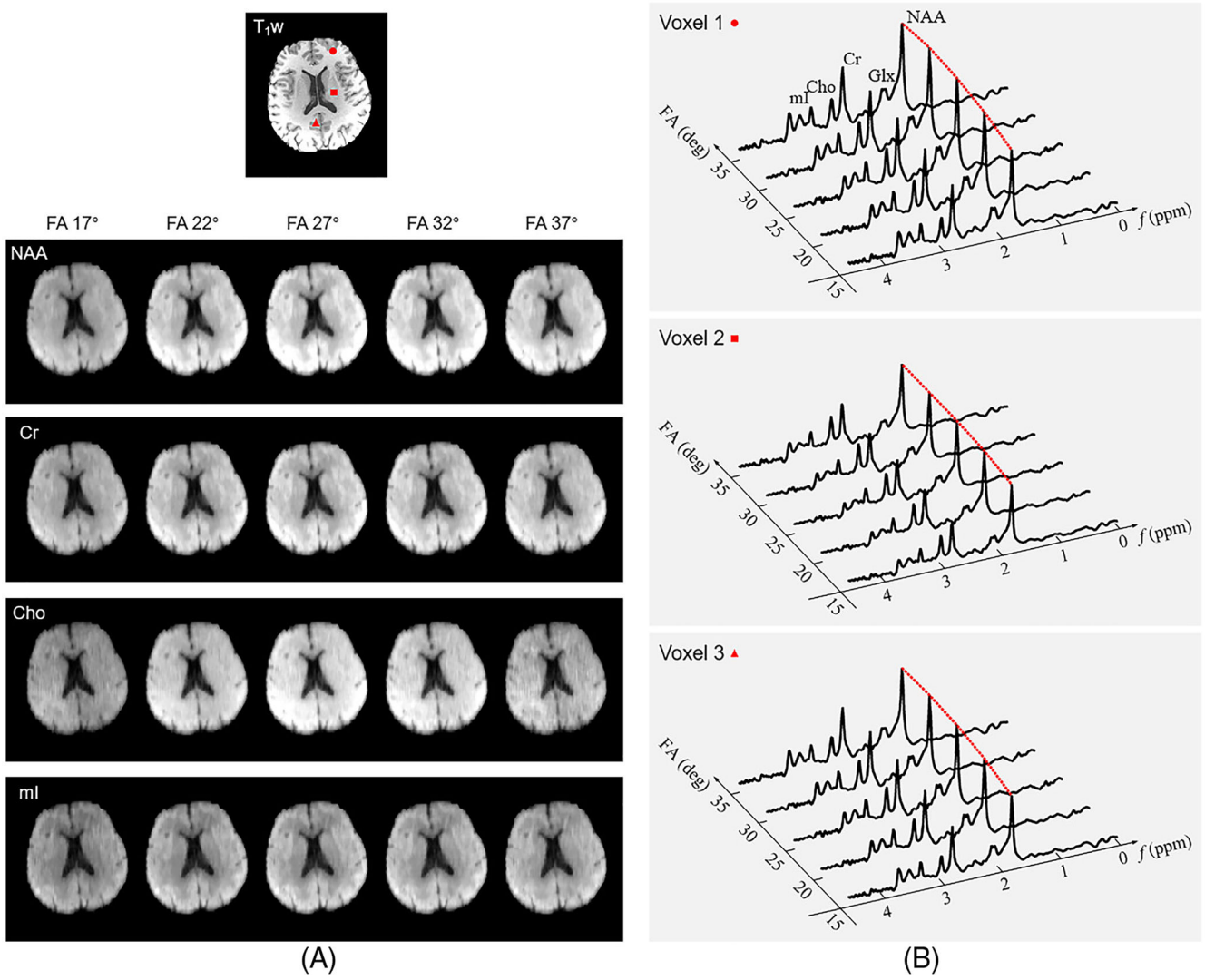

FIGURE 4.

Reconstructed variable-flip-angle (VFA) MRSI signals. (A) T_1-weighted anatomical image and reconstructed VFA N-acetylaspartate (NAA), creatine (Cr), choline (Cho), and myo-inositol (mI) maps. (B) Representative localized VFA spectra from three voxels, as indicated in the anatomical image. The metabolite maps and localized spectra were reconstructed with excellent SNR. FA, flip angle; T_1w, T_1-weighted.

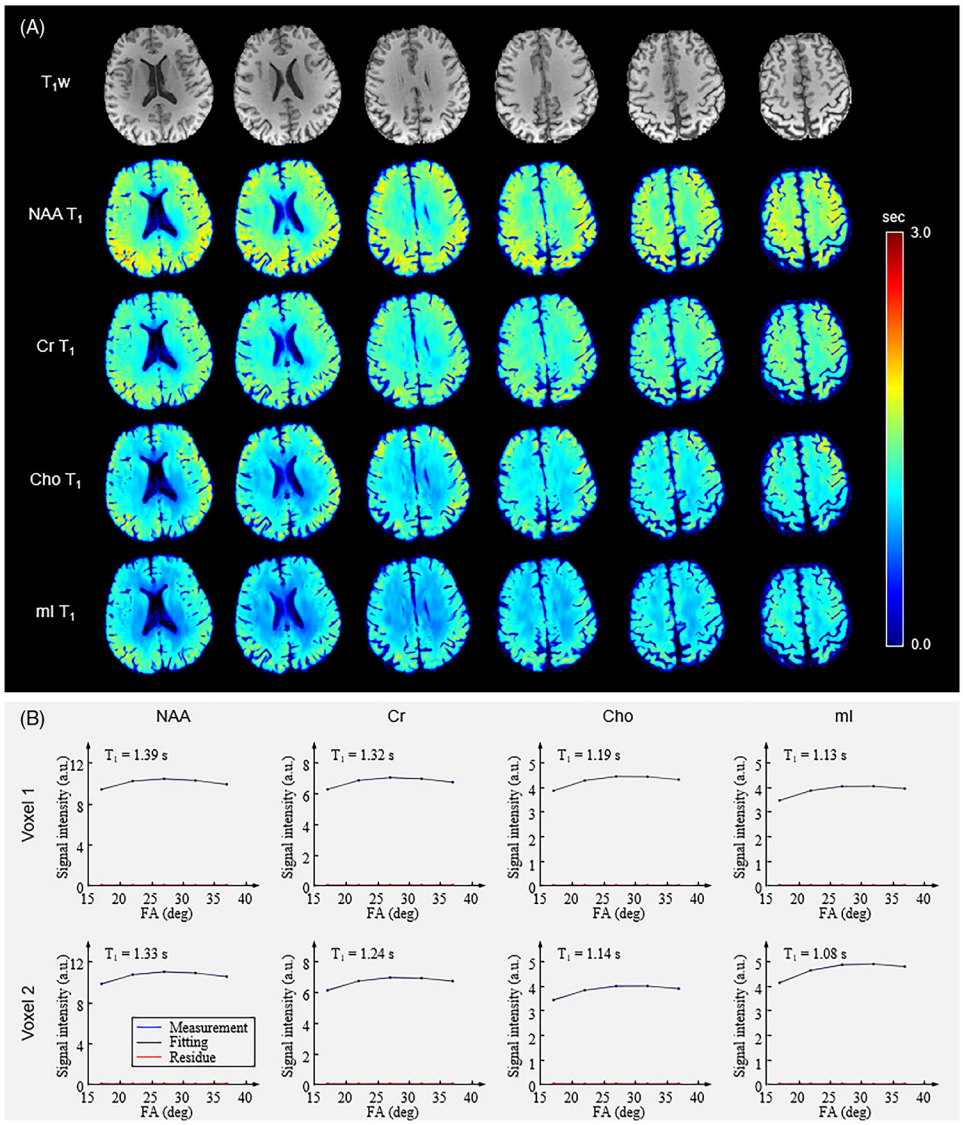

FIGURE 5.

T_1 fitting results of the reconstructed variable-flip-angle MRSI signals (CSF voxels excluded from fitting). (A) T_1-weighted (T_1w) anatomical image and metabolite T_1 maps. (B) Representative localized flip-angle curve fitting. The fitted T_1 maps exhibited large spatial coverage and high quality. The flip-angle curve fitting showed negligible residue. Cho, choline; Cr, creatine; FA, flip angle; NAA, N-acetylaspartate; mI, myo-inositol.

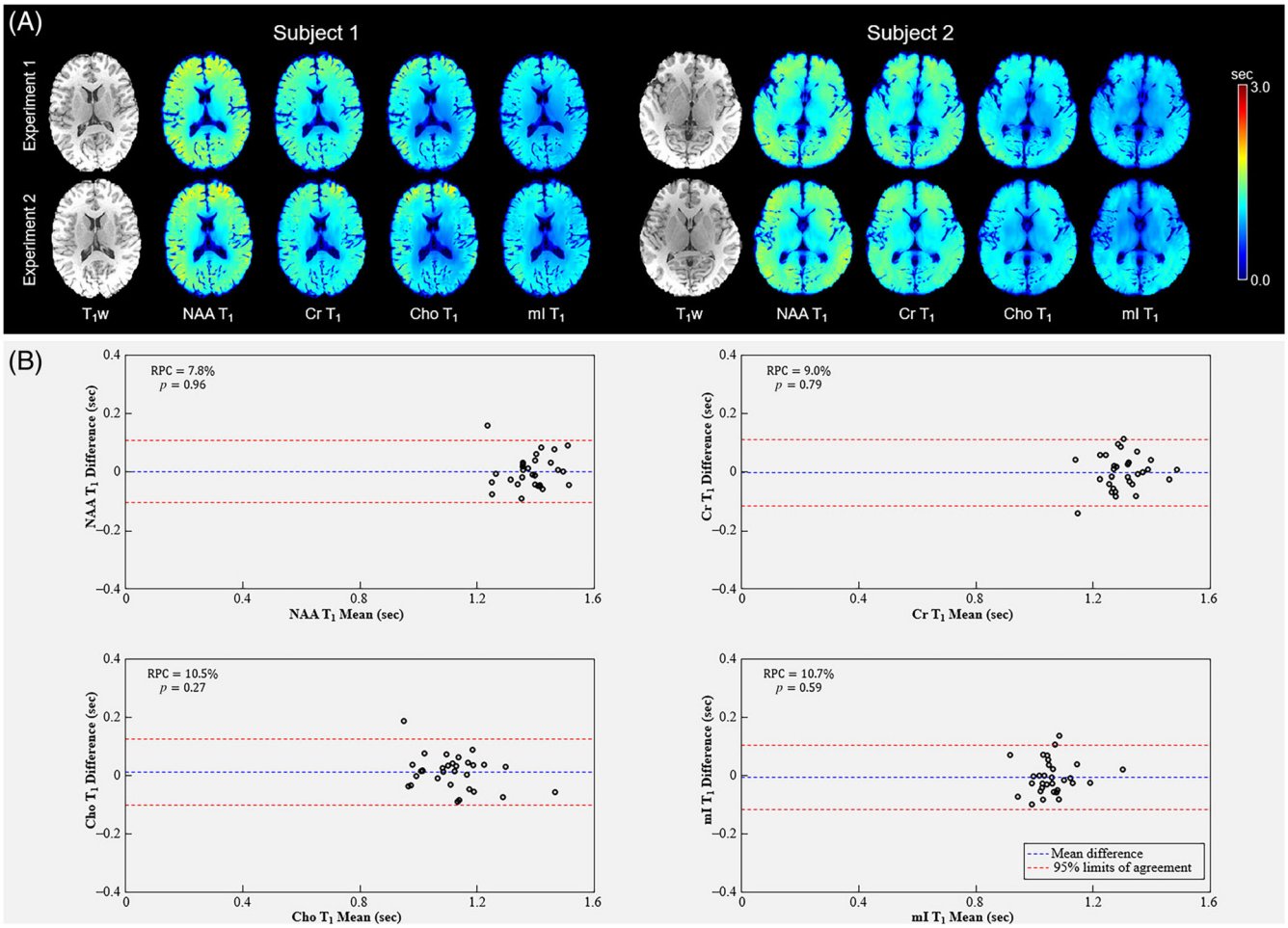

FIGURE 6.

Reproducibility study results. (A) T_1-weighted (T1w) anatomical image and metabolite T_1 maps obtained from 2 subjects in two experiment sessions (14 days apart). (B) Bland–Altman plots for N-acetylaspartate (NAA), creatine (Cr), choline (Cho), and myo-inositol (mI) T_1 values of 3 subjects in eight brain regions. The average sizes of these regions are frontal gray matter = 98.1 cm^3, frontal white matter = 100.9 cm^3, parietal gray matter = 87.4 cm^3, parietal white matter = 76.4 cm^3, temporal gray matter = 15.6 cm^3, temporal white matter = 7.7 cm^3, occipital gray matter = 13.3 cm^3, and occipital white matter = 6.8 cm^3. The metabolite T_1 maps exhibited good consistency between the two experiments. No significant biases were observed for the T_1 values of all molecules ($p > 0.05$).

TABLE 1

Metabolite and water T_1 values (mean ± SD in seconds) in gray-matter and white-matter regions obtained from the maps produced by the proposed method.

	Subject 1		Subject 2	
Brain regions and metabolites	**Experiment 1**	**Experiment 2**	**Experiment 1**	**Experiment 2**
Gray-matter NAA T_1	1.40 ± 0.17	1.42 ± 0.19	1.41 ± 0.13	1.44 ± 0.13
White-matter NAA T_1	1.32 ± 0.17	1.35 ± 0.18	1.32 ± 0.12	1.29 ± 0.11
Gray-matter Cr T_1	1.32 ± 0.13	1.32 ± 0.14	1.31 ± 0.12	1.28 ± 0.11
White-matter Cr T_1	1.25 ± 0.14	1.30 ± 0.13	1.34 ± 0.13	1.32 ± 0.11
Gray-matter Cho T_1	1.19 ± 0.17	1.14 ± 0.17	1.18 ± 0.13	1.10 ± 0.11
White-matter Cho T_1	1.03 ± 0.16	1.00 ± 0.16	1.04 ± 0.10	1.10 ± 0.08
Gray-matter mI T_1	1.06 ± 0.12	1.05 ± 0.12	1.02 ± 0.10	0.99 ± 0.12
White-matter mI T_1	1.02 ± 0.12	1.00 ± 0.11	1.02 ± 0.10	1.06 ± 0.12
Gray-matter water T_1	1.53 ± 0.11	1.52 ± 0.12	1.52 ± 0.12	1.53 ± 0.12
White-matter water T_1	0.93 ± 0.06	0.92 ± 0.05	0.93 ± 0.06	0.92 ± 0.05

Abbreviations: Cho, choline; Cr, creatine; mI, myo-inositol; NAA, N-acetylaspartate.